Experimental and numerical flow field study of submerged translating impinging inclined water jets

Bult, Sterre V.; Tokgoz, Sedat; Alhaddad, Said; Helmons, Rudy; Keetels, Geert H.

DOI
10.1017/flo.2025.10029

Publication date
2025

Document Version
Final published version

Published in
Flow

Citation (APA)
Bult, S. V., Tokgoz, S., Alhaddad, S., Helmons, R., & Keetels, G. H. (2025). Experimental and numerical flow field study of submerged translating impinging inclined water jets. *Flow*, *5*, Article E36. https://doi.org/10.1017/flo.2025.10029

Flow (2025), **5** E36
doi:10.1017/flo.2025.10029

FLOW CAMBRIDGE UNIVERSITY PRESS

RESEARCH ARTICLE

Experimental and numerical flow field study of submerged translating impinging inclined water jets

Sterre V. Bult[1], Sedat Tokgoz[2], Said Alhaddad[1], Rudy Helmons[1] and Geert H. Keetels[1]

[1]Section of Offshore and Dredging Engineering, Faculty of Mechanical Engineering, Delft University of Technology, Delft, 2628, The Netherlands
[2]Section of Ship Hydromechanics, Faculty of Mechanical Engineering, Delft University of Technology, Delft, 2628, The Netherlands
Corresponding author: Sterre V. Bult; Email: s.v.bult@tudelft.nl

Received: 16 March 2025; **Revised:** 30 July 2025; **Accepted:** 1 September 2025

Keywords: impinging jets; flow field; stereoscopic PIV; translating jets; CFD

Abstract

This study investigates the influence of multiple jet parameters on the flow field of translating impinging inclined water jets. We conducted full-scale stereoscopic particle image velocimetry and pressure measurements and three-dimensional computational fluid dynamics simulations for Reynolds numbers in the range of $Re = 23{,}000{-}43{,}750$. Considering the complex mechanism of a translating impinging jet, a good concordance is observed between the experimental and numerical results. The translation-to-jet velocity ratio (R) is identified as a critical parameter in determining whether the jet flow predominantly exhibits impinging characteristics or behaves as a jet in cross-flow. It is found that, for $R > 0.22$, jet impingement is minimal. The stand-off distance to nozzle diameter ratio (H/D) determines the relative influence of the cross-flow on the jet flow. The effect of H/D is similar to a stationary impinging jet, with the potential core extending up to $H/D \approx 4$, but entrainment is enhanced by the relative cross-flow. For an inclined jet, i.e. jet angle $\theta \neq 90^\circ$, the direction of the jet, either backward or forward, governs the deflection of the flow. Higher pressures are recorded for a backward directed jet compared with a forward directed jet for supplementary angles.

Impact Statement

The translating impinging jet is a complex phenomenon, as the flow characteristics are an interplay of wall-bounded flow and cross-flow effects. The existing research addresses both phenomena; however, they are consistently examined independently of one another. Understanding these fundamental processes is essential for accurately predicting shear stresses, pressure distributions and energy transfer mechanisms. This research combines experimental and numerical work to provide a description of translating impinging jet behaviour. We achieve this through an examination of flow velocities and streamlines, coherent structures and pressure distributions. These insights have broad implications for applications in aerospace, manufacturing and environmental engineering, where precise control over jet behaviour is critical for system performance.

1. Introduction

Research on impinging jets is considerable due to its numerous engineering applications, including heating and cooling, rocket engines, waste disposal, water jet cutting and hydraulic works. The instantaneous flow field is valuable input for predicting sediment erosion, as it provides critical insights into turbulence,

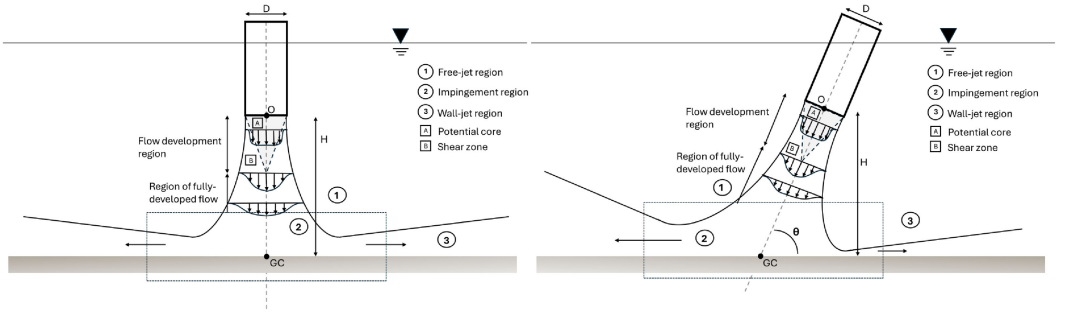

Figure 1. *Flow development of a vertical (left) and inclined (right) circular stationary submerged jet impinging on a flat surface, taken from Alhaddad et al. (2025).*

shear stresses and pressure fluctuations at the impingement site. Understanding these flow characteristics is essential for translating jet applications across various industries, including water injection dredging (Van Raalte and Bray, 1999), the discharge of trailer suction hopper dredgers (de Wit *et al.*, 2015), jet trenching (Zhang *et al.*, 2024), jetting in clay (Nobel, 2013), sand blasting (Oranli *et al.*, 2023) and rock drilling (Lu *et al.*, 2013). The flow characteristics of a translating impinging jet are a combination of a jet in cross-flow and a stationary impinging jet. Studies describing both phenomena separately have been extensive. Yet, research on the flow field of translating impinging jets is extremely limited. As many applications use translating jets in contact with a substrate, it is crucial that the flow field is studied to bridge the gap between the two phenomena.

As described above, the translating impinging jet is a complex phenomenon, with its characteristics being governed by a combination of the presence of the bed and a cross-flow resulting from its motion through the medium. The jet in cross-flow, i.e. transverse jet, has received considerable attention due to its wide application, including natural phenomena and gas-turbine combustors (Mahesh, 2013). The majority of this research focuses on transverse jets protruding from a wall, which create an interaction with the wall boundary layer. The four coherent structures in the near field of the flush transverse jet are: (i) jet shear-layer vortices, (ii) the wake vortices, (iii) horseshoe vortices and (iv) the counter-rotating vortex pair (CVP). Of these structures, the horseshoe vortices and CVP have a mean-flow definition (Fric and Roshko, 1994). The CVP is the dominant vortical structure in the wake and has been shown to contribute significantly to the jet's mixing characteristics (Gevorkyan *et al.*, 2016). Its formation is delayed as the jet-to-cross-flow velocity ratio, R, increases (Smith and Mungal, 1998). Huang and Hsieh (2003), by studying elevated jets, suggested that, below a critical value of R, the jet is dominated by the cross-flow, whereas for high values of R, the jet dominates the flow. In research on the jet in cross-flow, the convention is to use the jet-to-cross-flow velocity ratio. On the other hand, translating jet studies use the translation-to-jet velocity ratio and we will use this ratio hereafter. However, the two relations are their own inversion and provide a ratio between the two velocities.

Flow field studies on impinging jets have primarily focused on stationary jets. The flow field of an impinging jet consists of three distinct regions: the free-jet region, the impingement region and the wall-jet region (figure 1, left). In the free-jet region, a shear layer forms between the jet and the ambient water, diminishing the potential core. The flow transitions to a fully developed jet flow, provided that the distance between the jet exit and the bed is sufficient. In fully developed jet flow, there is an established relationship between the rates of velocity decay and jet growth. The impingement region is characterised by a strong deceleration of the flow velocity and pressure rise. Impingement on the surface potentially causes erosion and deformation of the surface. The flow deflects parallel to the surface and the pressure drops to ambient values in the wall-jet region.

The flow field of stationary vertical impinging jets has been generally well described. By conducting experiments using laser-Doppler velocimetry, Fitzgerald and Garimella (1998) showed that an increase in bed-to-nozzle spacing H/D, with H being the height of the nozzle exit to the bed and D the nozzle diameter, is related to a reduction in the magnitudes of the radial velocities in the impingement

https://doi.org/10.1017/flo.2025.10029 Published online by Cambridge University Press

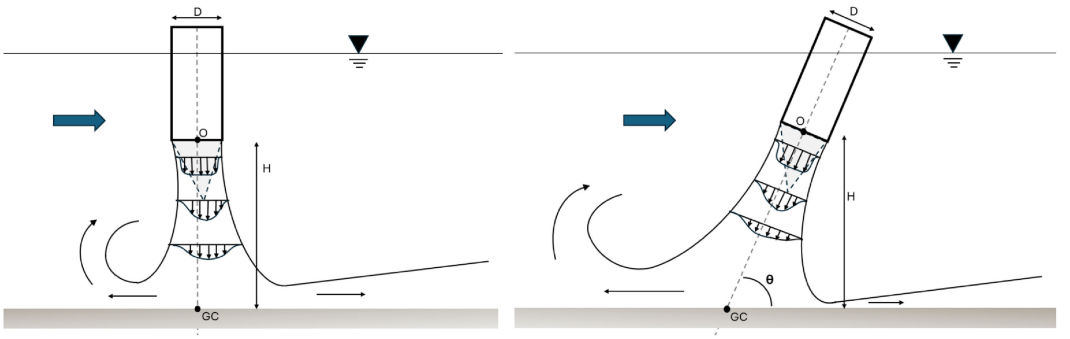

Figure 2. *Flow development of a vertical (left) and forward inclined (right) circular submerged translating jet impinging on a flat surface. The blue arrows indicate the direction of the relative cross-flow. The jet translates in the opposite direction, from right to left.*

and wall-jet regions, as well as a decrease in peak turbulence intensities for Reynolds numbers in the range Re = 8500–23,000. This is in agreement with the work by Hammad and Milanovic (2011), who conducted particle image velocimetry (PIV) measurements for Re = 15,895 and H/D = 1–8. Not only the flow patterns, but also the jet impact forces ,highly depend on the nozzle-to-bed distance H/D, with the mean impact force coefficient exhibiting a linear relation with H/D (Wang *et al.*, 2015). The slope of the variation of the jet impact is dependent on the range of H/D, where the steepest slope is observed for $4 < H/D < 14$. The same study showed that the flow patterns and forces are relatively insensitive to the Reynolds number within the examined range (Re = 9800–46,550). In addition, Hassan *et al.* (2013) found that wall shear stress is predominantly influenced by the dynamics of the large-scale vortical structures and their separation near the impinging wall by using time-resolved particle image velocimetry measurements and the polarographic method.

For vertical circular jets the flow can be assumed to be axisymmetric. However, this is not the case for inclined jets (Beltaos, 1976). The flow is expected to be symmetric about the jet centreline, but the flow distribution between the uphill and downhill regions depends on the jet inclination (Mishra *et al.*, 2020). The flow development for an inclined jet is shown in figure 1 (right). This study also shows that the flow distribution depends on H/D for inclined jets. Wang *et al.* (2017) reports that energy loss of the jet in the process of impingement is found to increase with the jet angle θ and that the maximum pressure coefficient is found for a vertical jet ($\theta = 90°$). These experimental results were used by Zhang *et al.* (2022) to validate a computational fluid dynamics (CFD) model to study the influence of H/D on the flow field characteristics. They found that the effective impingement area does not change for H/D in the range 1–8. When the impinging jet is translating as well, the flow will be affected by the relative cross-flow (figure 2). The jet centreline will deflect towards the leeward side and the wall jet on the windward side will be pushed backwards by the cross-flow. Note that we superpose translation and cross-flow, so relative cross-flow is equal to translation of the jet. For CFD, we hypothesise that the difference between a translating jet in a stagnant ambient fluid and a stationary jet in cross-flow is negligible. Yet, a translating jet is more complex to operate in experimental conditions and thus more prone to errors.

While multiple erosion studies have reported the importance of the translation-to-jet velocity ratio R for the erosion depth (Dong *et al.*, 2020; Yeh *et al.*, 2009; Zhang *et al.*, 2016) and Alhaddad *et al.* (2025) suggested a difference in deflection for supplementary jet angles, the flow field for representative jetting velocities has not been studied. Therefore, the objective of this study is to investigate the effect of jet velocity, translation velocity, angle of inclination and stand-off distance on the flow field of jets impinging on a wall. To this end, we conducted full-scale stereoscopic PIV measurements with a state-of-the-art underwater PIV set-up. The velocity fields were complemented by pressure measurements. As the stereo-PIV measurements are limited to two-dimensional (2-D) measurements with out-of-plane velocity components, the experimental results are complemented by 3-D CFD simulations in OpenFOAM.

https://doi.org/10.1017/flo.2025.10029 Published online by Cambridge University Press

We show how the flow field and coherent structures, as well as the bed pressure distribution, are affected by the different jet parameters.

2. Dimensional analysis of a translating impinging jet

An impinging jet will give rise to a pressure field at the bed by the strong deceleration of the flow. Translation of the jet creates a relative cross-flow and the jet stream will deflect, which will affect the pressure distribution and maximum pressure on the bed. To investigate the effect of the relative cross-flow as well as the jet parameters on the maximum dynamic pressure, a dimensional analysis was conducted using the Buckingham π theorem (Liu *et al.*, 2023). Besides the translational velocity and the jet parameters, the pressure is also influenced by the water density and kinematic viscosity. The function that describes the dynamic pressure at the bed is defined as

$$P = f\left(\rho, \mu, U_t, V_b, D, H, \theta\right) \tag{2.1}$$

where P is the dynamic pressure, ρ is the water density, μ is the kinematic viscosity, U_t is the translating velocity, V_b is the bulk jet exit velocity, defined as the mean velocity over the jet exit, D is the nozzle diameter, H is the stand-off distance to the bed and θ is the angle of incidence. The basic quantities were chosen to be ρ, D and V_b, which resulted in the following five dimensionless parameters:

$$\pi_0 = \frac{P}{\frac{1}{2}\rho V_b^2}; \quad \pi_1 = R = \frac{U_t}{V_b}; \quad \pi_2 = \frac{H}{D}; \quad \pi_3 = \theta; \quad \pi_4 = \frac{\mu}{\rho D V_b} = \frac{1}{Re}. \tag{2.2}$$

Thus, the dimensionless pressure coefficient, $C_p = \pi_0 = \frac{P}{\frac{1}{2}\rho V_b^2}$, can be expressed as follows:

$$C_p = f\left(R, \frac{H}{D}, \theta, \frac{1}{Re}\right). \tag{2.3}$$

Multiple studies have shown that the pressure coefficient is relatively insensitive to the Reynolds number in the range Re = 9800–46,550 (Wang *et al.*, 2017; Wang *et al.*, 2015; Zhang *et al.*, 2022). As our jet parameters studied fall within this range, we have not incorporated this dimensionless parameter in our study. However, for jet studies with Reynolds numbers significantly higher or lower, the effect can be substantial (Deo *et al.*, 2008). In our study, the jetting fluid was the same as the surrounding fluid, namely fresh water. Considering air jets in air will affect the jet Reynolds number, with a potential shift in jet regime as a result. Besides, if the jetting fluid and surrounding fluid properties are different, mixing with the ambient fluid will be minimal. This might have consequences for the observed jet mechanisms (Jalil and Rajaratnam, 2006). For example, the wall-jet-like profiles will not develop for non-submerged jets.

3. Experimental set-up

Experimental investigations were carried out on the small towing tank of the Ship Hydromechanics Laboratory at Delft University of Technology, which measures 85 m in length and 2.75 m in width, with a maximum water depth of 1.25 m. A carriage running on rails at the sides of the tank was used to mount the nozzle and the PIV system. For the current set-up, the maximum carriage speed was 2 m s^{-1} to limit the vibrations during the experiments. Different nozzles were 3D printed in resin to limit alterations made to the general set-up. The nozzles were fabricated using stereolithography, with a resolution of 0.1 mm. Each nozzle was mounted to a 80 × 80 mm Item profile with wing-shaped attachment pieces in front to minimise its drag effect on the jet flow velocities. The immersion depth of the nozzle was over 600 mm to ensure a negligible effect of the free surface.

The base case consisted of a nozzle with inner diameter of 5 mm, an inclination angle of 90° relative to the bed and a stand-off distance of 3 cm (6D). In addition, two nozzles with angles of 60° and 30° (120° and 150° in the backward direction) and a nozzle with a stand-off distance of 6 cm (12D) were

https://doi.org/10.1017/flo.2025.10029 Published online by Cambridge University Press

Table 1. *A summary of the experiments conducted in this study.*

Test #	V_b [m s^{-1}]	U_t [m s^{-1}]	θ [°]	H [cm]	R [–]	H/D [–]	Re [–]
1	8.75	1.0	90	3	0.11	6	43,750
2	8.75	2.0	90	3	0.23	6	43,750
3	4.60	1.0	90	3	0.22	6	23,000
4	4.60	2.0	90	3	0.43	6	23,000
5	4.60	1.5	90	3	0.33	6	23,000
6	8.75	1.0	60	3	0.11	6	43,750
7	8.75	1.0	30	3	0.11	6	43,750
8	8.75	1.0	120	3	0.11	6	43,750
9	8.75	1.0	150	3	0.11	6	43,750
10	8.75	1.0	90	6	0.11	12	43,750

tested. The inner profile of the nozzles was not a tube, as some other studies utilised (Wang *et al.*, 2017), but all nozzles had a convergent internal profile. No additional upstream flow conditioning was applied. Especially the inclined jets had a short straight length due to a bend in the profile. Generally, this is not considered sufficiently long to produce a fully developed turbulent flow (Schlichting, 1979). While the throat lengths were sufficient for a high discharge coefficient (Jiang *et al.*, 2022), the jet exit velocity profile and turbulence intensity at the jet exit, amongst other things, might have differed slightly from a fully developed jet flow. The jet fluid was provided by a positive displacement pump, with flow rates varying between 5.4 and 12.0 l min^{-1}, resulting in jet bulk velocities of V_b = 4.6 and 8.8 m s^{-1}. The corresponding jet Reynolds numbers Re ($= \frac{V_b D}{\nu}$, where ν is the kinematic viscosity of water) were 23,000 and 43,750, respectively. Lastly, the translating velocities ranged from 1 to 2 m s^{-1}, thus the translation-to-jet velocity ratios R were 0.11–0.43. An overview of all test conditions is provided in table 1. All jets were impinging on a table, with dimensions 9 m x 50 cm x 30 cm. The impingement table was fixed in place at the bottom of the towing tank and divided into two adjacent sections. One section was prepared with epoxy and black lacquer, which allows us to make the assumption of a hydraulically smooth surface. The second section was also prepared with a thin black lacquer layer, but in addition, fine sand particles (Sibelco Silica MI 0.1–0.35 DS, D_{50} = 0.27 mm) were added. Therefore, this section was assumed to be hydraulically rough.

3.1. Particle image velocimetry set-up

An underwater stereo PIV system measured the velocity fields of the impinging water jet (figure 3) in a vertical plane parallel to the direction of the jet's translation. The stereo PIV set-up enables the measurement of the out-of-plane component of the velocity vector within the same plane, which is preferable over planar PIV measurements as the circular jet is highly three-dimensional. However, due to reflections and a limited number of particles, the quality of the stereoscopic measurements was lower than we anticipated, particularly near the table surface. As a result, we chose to rely solely on 2-D PIV measurements for this study. The cameras were located in a watertight torpedo-shaped housing, with each camera section looking at the field of view under a 60° angle (Jacobi *et al.*, 2019), with the camera sections being 1040 mm apart. The horizontal stand-off distance to the field of view was approximately 1150 mm. The measurement plane was illuminated with a Litron Nd:YAG laser with an energy of 50 mJ pulse^{-1} at a wavelength of 532 nm, with each of the two cavities having a maximum repetition rate of 50 Hz (Jacobi *et al.*, 2022). The laser head and first mirror section were placed above water, whereas the second mirror section was placed underwater behind the water jet in a separate torpe do. The distance between the laser torpedo and the nozzle was approximately 700 mm. This allows for recording of the longitudinal plane with minimal obstruction by the nozzle, while ensuring sufficient

https://doi.org/10.1017/flo.2025.10029 Published online by Cambridge University Press

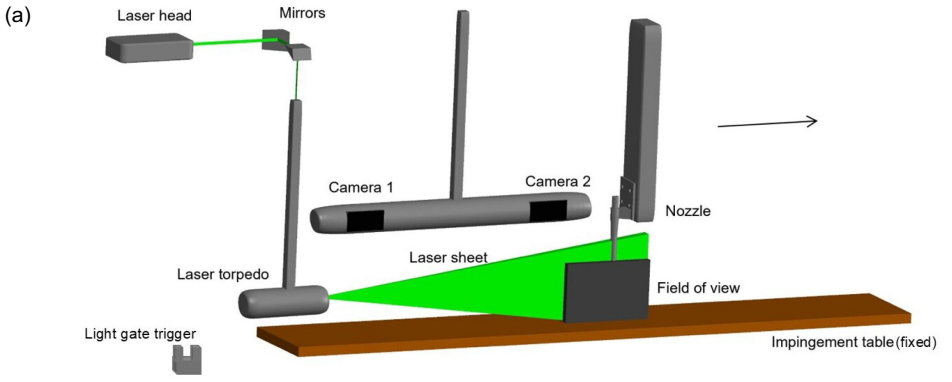

Schematic drawing of the PIV setup. The arrow indicates the translation direction.

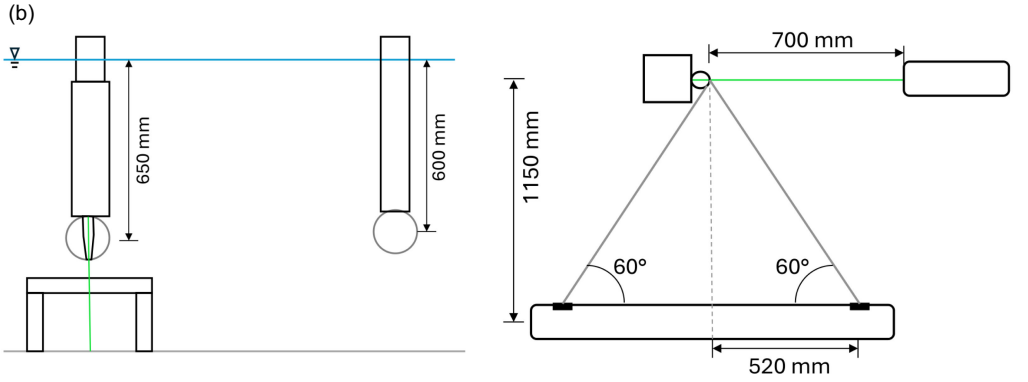

Dimensions of the PIV setup for the front view (left) and top view (right).

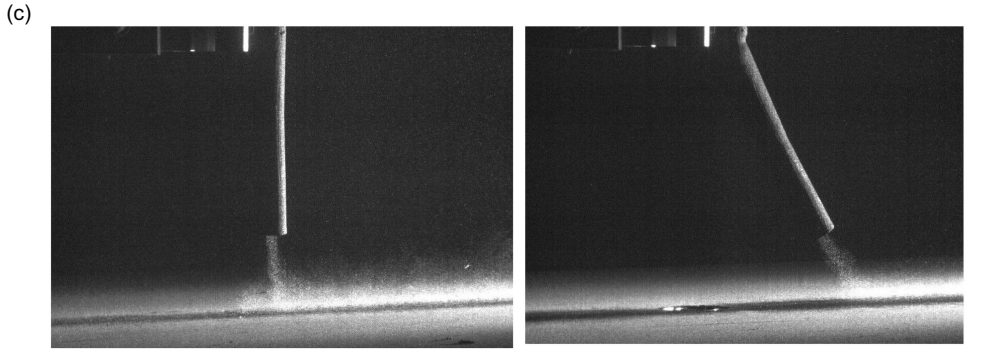

Raw PIV images for a vertical nozzle (left) and an inclined nozzle with a jet angle of 60° (right).

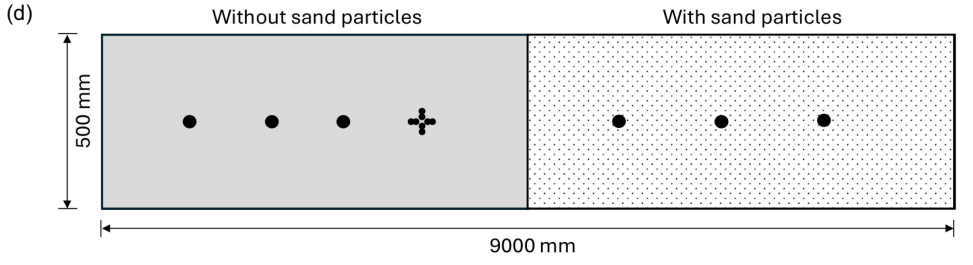

Top view of the impingement indicating the roughness sections and the approximate location of the pressure sensors.

Figure 3. *Schematic overview of the experimental PIV set-up.*

https://doi.org/10.1017/flo.2025.10029 Published online by Cambridge University Press

laser power at the field of view. The laser sheet thickness was approximately 5 mm at the location of the nozzle. The torpedoes had an immersion depth of 600 and 650 mm for the camera and laser torpedo, respectively.

Image acquisition and processing were performed using DaVis software by LaVision. Images were recorded in a double frame mode with two LaVision Imager M x 4 M cameras with a CCD sensors size of 2048 × 2048 pixels. The pixel size is 5.5 μm. The cameras were equipped with lenses with a 50 mm focal length. The resulting field of view was approximately 200 × 200 mm^2, with a digital resolution of 9.2 pixels $(mm)^{-1}$. The final area of interest was 150 × 50 mm^2 to capture the entire flow field of each water jet. Additionally, the Scheimpflug angle and f-numbers were $8.0°$ and $-7.0°$ and 16 and 13.4 for cameras 1 and 2, respectively. The estimated depth of focus for both cameras was approximately 4 cm. The number of image pairs per table section was 220 for the lowest speed and 110 for the highest speed. Multiple experimental runs were performed for each test condition to obtain at least 400 image pairs per section. Analysis of the jet core mean-flow velocities showed that 400 image pairs are sufficient to achieve convergence of the mean flow. Significantly more image pairs are required for statistical convergence of turbulence. However, this did not align with the capabilities of the current experimental set-up and was beyond the scope of the current study. The exposure time delay between image pairs was either 70 or 140 μs, depending on the jet exit velocity. This resulted in an approximate particle displacement of 4–6 pixels. Calibration of the stereo PIV system was achieved by using a two-level double-sided calibration plate (310 × 310 mm), which was mounted to the nozzle strut and aligned with the jet axis in the translation direction. The flow was seeded with spherical polymer particles with a mean diameter of 50 μm, primarily from the tank supplying fluid to the nozzle. This enables the capture of the full jet velocity field. The quantity of seeding particles in the towing tank was lower compared with the jet fluid. As the jet velocity field was of main interest, no additional seeding material was added to the towing tank.

During the preparation of the experimental set-up, black paint was applied to the nozzle, table and sand to minimise laser reflections. This black paint significantly reduced unwanted reflections from both the nozzle and the table in the images, although it did not eliminate them entirely, meaning the painted parts still exhibited reflection. This is a common concern in the areas close to solid surfaces for all PIV implementations (Adrian and Westerweel, 2011; Jacobi *et al.*, 2022; Paterna *et al.*, 2013). The entire set-up was also subject to small vibrations due to drag and translation of the whole set-up, which further increased the uncertainty. Optical imperfections of the underwater torpedoes also made it difficult to do the stereoscopic alignment. To further reduce background noise and enhance image quality, image pre-processing was conducted after data acquisition. Initially, a geometric mask was applied to exclude the nozzle and table from the images. Subsequently, a sliding minimum intensity subtraction was performed over a 7×7 pixel area on all images to improve the signal-to-noise ratio. Then, velocity vectors were calculated using multi-pass approach. The interrogation window size was 32×32 pixels with a 50% overlap in the first pass, and 24×24 pixels, with a window overlap of 75% in the final three passes. Detection and removal of the spurious vectors were done by the universal outlier detection method (Westerweel and Scarano, 2005). Uncertainties in the jet core mean velocity were around 10% for test condition 1 due to the relatively low-quality images.

Both the jet and PIV imaging system, attached in the same carriage structure, were moving at a constant translating velocity over the fixed table. The carriage was accelerated from a standstill to the target velocity, which was reached in good time within the acceleration section of 20 m before the start of the table. The carriage speed was monitored during the experiments, and shown to be constant for all conditions. A light gate trigger then initiated the PIV and pressure measurements, which was positioned at 1.87 m from the start of the table. Only the images from a fully developed impinging jet were considered for the PIV analysis, thus the startup of jet impingement at the beginning of the table was not included. Weights were attached to the table to minimise movement during passing of the jet and PIV system.

https://doi.org/10.1017/flo.2025.10029 Published online by Cambridge University Press

3.2. Pressure measurements

The pressure field was recorded with piezoresistive flush-diaphragm 19 mm diameter pressure transmitters (Keller PA-9L, with a measurement range of 1 bar, accuracy of 0.25% of the full scale and typical sensitivity of 80 mV (mA x bar)$^{-1}$). In addition, 8 miniature pressure sensors (SMI, SM5420E Series) with a port diameter of 0.4 mm were placed in a cross shape to allow for the measurement of the pressure distribution in the jet flow (figure 3d). Potential air bubbles in the miniature pressure sensors were removed by placing a vacuum pump over the ports before the measurements. No deterioration in the sensor functionality due to the potential intrusion of seeding particles was observed during the measurement period. The sample rate for all pressure measurements was 10 kHz. We chose to utilise two different sensors, as the Keller sensors allowed for precise averaged measurements, while the miniature sensors record maximum bed pressure with a larger error margin. All pressure sensors were flush mounted in the impingement table. Three Keller sensors and the miniature sensors were mounted in the hydraulically smooth section of the table. In addition, three Keller sensors were mounted in the hydraulically rough sections. For each set of sensors, i.e. the two sets of Keller sensors and the four miniature sensors at the jet centreline, the maximum values were averaged over all runs per condition. The maximum values of the Keller sensors were overall lower than those measured by the miniature sensors, as the Keller sensors average the pressure over the diaphragm.

4. Numerical model

4.1. Turbulence model

The $k-\omega$ SST turbulence model was chosen, as the $k-\omega$ models are most suitable for wall-bounded flows, such as the impinging jet flow (Liu *et al.*, 2023). For the jet in cross-flow, the realisable $k-\epsilon$ turbulence model is often chosen, but the Reynolds-averaged Navier–Stokes (RANS) models generally underpredict the turbulence intensity and the strength of the CVP (Coletti *et al.*, 2013; He *et al.*, 1999). However, large eddy simulation (LES) models (de Wit *et al.*, 2014) are not preferred for our application as they require high computational effort. The translating impinging jet involves both wall-bounded flow and cross-flow, requiring a turbulence model that captures near-wall effects and free-stream mixing. The $k-\omega$ SST model achieves this by using $k-\omega$ near the wall for accuracy in boundary layers and transitioning to $k-\epsilon$ further away for better turbulence prediction. The equations for the turbulence kinetic energy k and specific dissipation rate ω are defined as (Menter, 1994)

$$\frac{\partial}{\partial t}(\rho k)+\frac{\partial}{\partial x_i}(\rho k u_i)=\frac{\partial}{\partial x_j}\left(\Gamma_k\frac{\partial k}{\partial x_j}\right)+\tilde{G}_k-Y_k+S_k, \tag{4.1}$$

$$\frac{\partial}{\partial t}(\rho\omega)+\frac{\partial}{\partial x_i}(\rho\omega u_i)=\frac{\partial}{\partial x_j}\left(\Gamma_\omega\frac{\partial \omega}{\partial x_j}\right)+G_\omega-Y_\omega+D_\omega+S_\omega, \tag{4.2}$$

where $\tilde{G}_k$ and G_w represent the generation of k due to mean velocity gradients and ω, Γ_k and Γ_ω the effective diffusivity of k and ω, Y_k and Y_ω the dissipation due to turbulence, D_ω the cross-diffusion term and S_k and S_ω are user-defined source terms.

4.2. Grid and boundary conditions

A 3-D grid was created with the blockMesh utility in OpenFoam, which represents the tank containing the submerged impinging jet. The dimensions of the tank were $80D$, $40D$ and $20D$ for the length, width and height, respectively. The domain is sufficiently large for the influence of the walls to be minimal, especially for a translating jet. To implement the jet, nozzle STL files were created that were incorporated into the blockMesh grid with the snappyHexMesh utility. The nozzles were surrounded by an additional geometry to mimic the material thickness of the nozzles fabricated for the experiments. To reduce the computational time, the grid was refined towards the jet exit in the x- and z-directions as well as towards the bed in the y-direction with a factor 4. The numerical grid for the vertical jets is shown in figure 4.

https://doi.org/10.1017/flo.2025.10029 Published online by Cambridge University Press

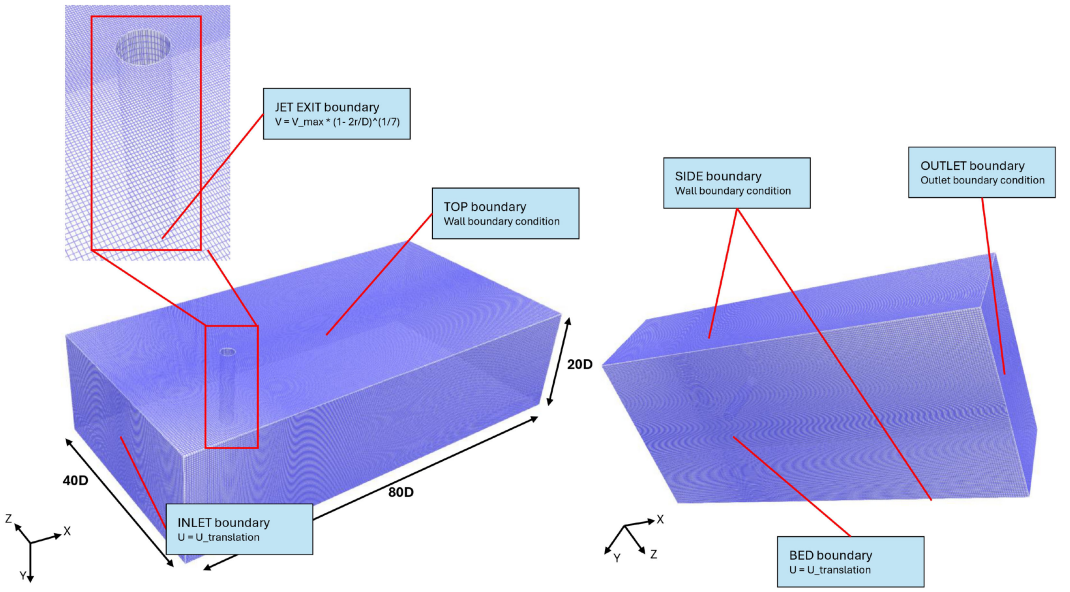

Figure 4. *Base numerical grid with the names of the boundary conditions. The bottom figures show the entire domain, while the top figure shows the nozzle with its velocity boundary condition indicated.*

For the inclined nozzles the set-up was similar, but naturally the geometry was adjusted to allow for the angle. The grid refinement was adjusted accordingly.

The computational mesh consists of approximately 6.2 million cells. To test the solution's dependence on the spatial resolution, both a coarser and finer mesh were considered. The coarser mesh had approximately 4.3 million cells, which represents a 1.13 times coarser grid. The finer grid had a 1.25 times increase in the number of cells in each direction, resulting in approximately 12.2 million cells. As the jet exit velocity and pressure profile at the bed are both important parameters, these were compared for the different mesh sizes. The jet exit velocity did not show significant differences when varying the mesh size. However, the maximum bed pressure was slightly lower for the coarsest mesh compared with the medium and fine mesh. Therefore, it was revealed that the medium mesh with 6.2 million cells was sufficient to have a reliable solution while being relatively computationally efficient.

The nozzle geometry is fixed in place, and a constant velocity is imposed at the inlet. The bed moves with the same velocity. This mimics the movement of the nozzle through the water medium. The imposed velocity depends on the chosen translation velocity. The velocity at the jet exit was defined by the empirical power law for a fully developed jet exit velocity

$$\frac{V}{V_{max}} = \left(1 - \frac{2r}{D}\right)^{1/n}, \tag{4.3}$$

where V is the axial velocity, V_{max} is the maximum jet velocity ($\approx 1.2V_b$) and n is an empirical constant. The exit velocity of a fully developed turbulent jet can be approximated by the 1/7th power law (Fairweather and Hargrave, 2002). Besides the outlet, where the pressure was to be equal to the internal field, all boundaries had a zero gradient pressure condition. The turbulence intensity k at the outer boundaries was chosen to be 0.01, while it was equal to the internal field at the nozzle geometry. A higher k-value of 0.05 was also tested for the nozzle geometry, as it was uncertain how the different geometries and the 3D printing tolerance, especially for these relatively small geometries, affected the turbulence intensity at the jet exit. A higher k-value resulted in a slightly shorter potential core and lower bed pressure, with the latter observation not being consistent with the pressure measurements. Therefore, the internal field was chosen to be the representative turbulence intensity.

https://doi.org/10.1017/flo.2025.10029 Published online by Cambridge University Press

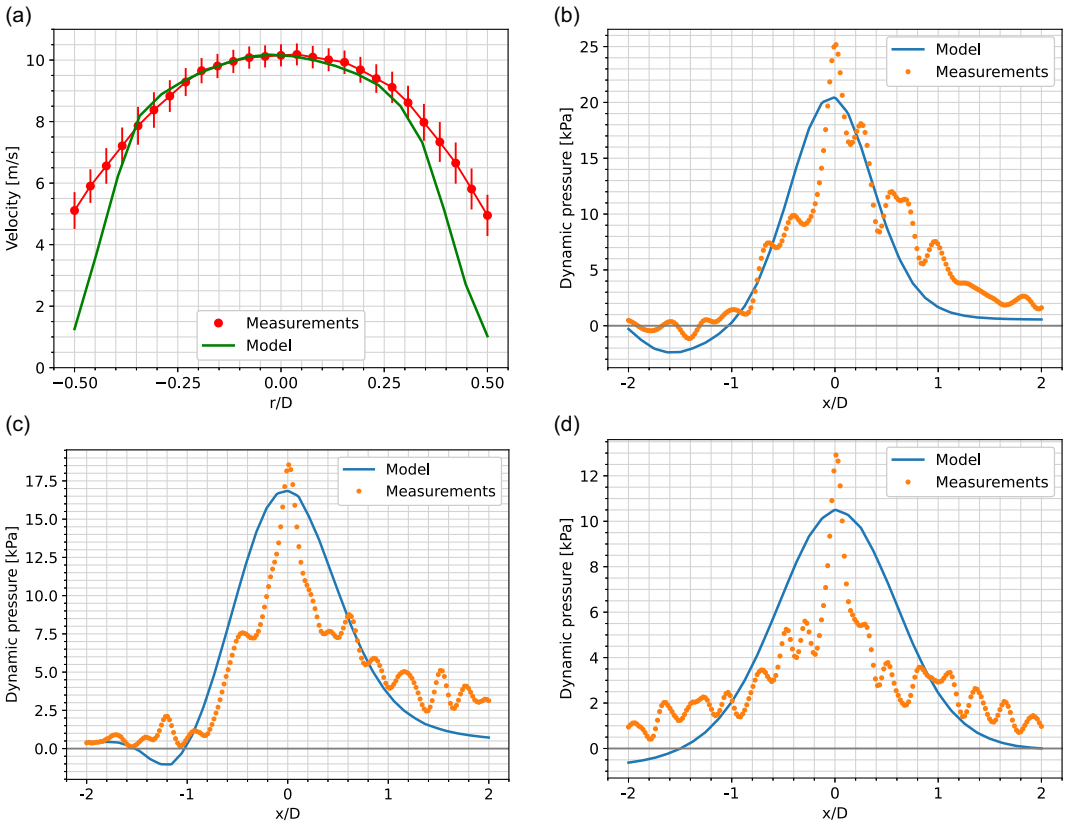

Figure 5. *Comparison of the averaged jet exit velocity profile at $y/D = 0$ between model and experiments (a). Besides the velocity comparison, the dynamic pressure profile in longitudinal direction at the jet centreline of both the model and experiments are shown for test condition 1 (b) ($R = 0.11$ and $\theta = 90°$), as well as for (c) condition 6, $R = 0.11$ and $\theta = 60°$ and (d) condition 8, $R = 0.11$ and $\theta = 120°$.*

4.3. Model comparison

The model was compared with the experimental results to evaluate its behaviour and overall performance. The jet exit velocity profile and jet centre bed pressure profile in the longitudinal direction were chosen as the parameters of comparison. For test condition 1, the base case, the model jet exit velocity matches the magnitude and profile of the PIV measurements well (figure 5a). The model profile and the integrated PIV profile show minimal differences. Both have been linearly integrated at the jet exit. The PIV profile shows higher values at the outer edges, where the velocity value is an integration of the high jet velocities and the relatively stagnant ambient fluid. Correspondingly, the standard error of the measured velocity is smallest at the jet centreline, and increases towards the outer edges. In figure 5b, the bed pressure profile for the same test condition is shown. The model is able to reproduce the spread and pattern of the pressure profile, even though the maximum bed pressure is slightly lower. The pattern of the pressure profile is also modelled generally well for the backward (figure 5c) and forward (figure 5d) directed jets. The spread of the peak bed pressure is slightly overestimated by the model, where the measurements show a very sharp peak bed pressure. While the model satisfies the criteria at the jet exit and bed boundary, we also observe differences. However, since the model is based on fundamental physical laws and we employ appropriate mathematical techniques and procedures, the steady-state RANS model remains a suitable approach for modelling translating impinging jet conditions.

https://doi.org/10.1017/flo.2025.10029 Published online by Cambridge University Press

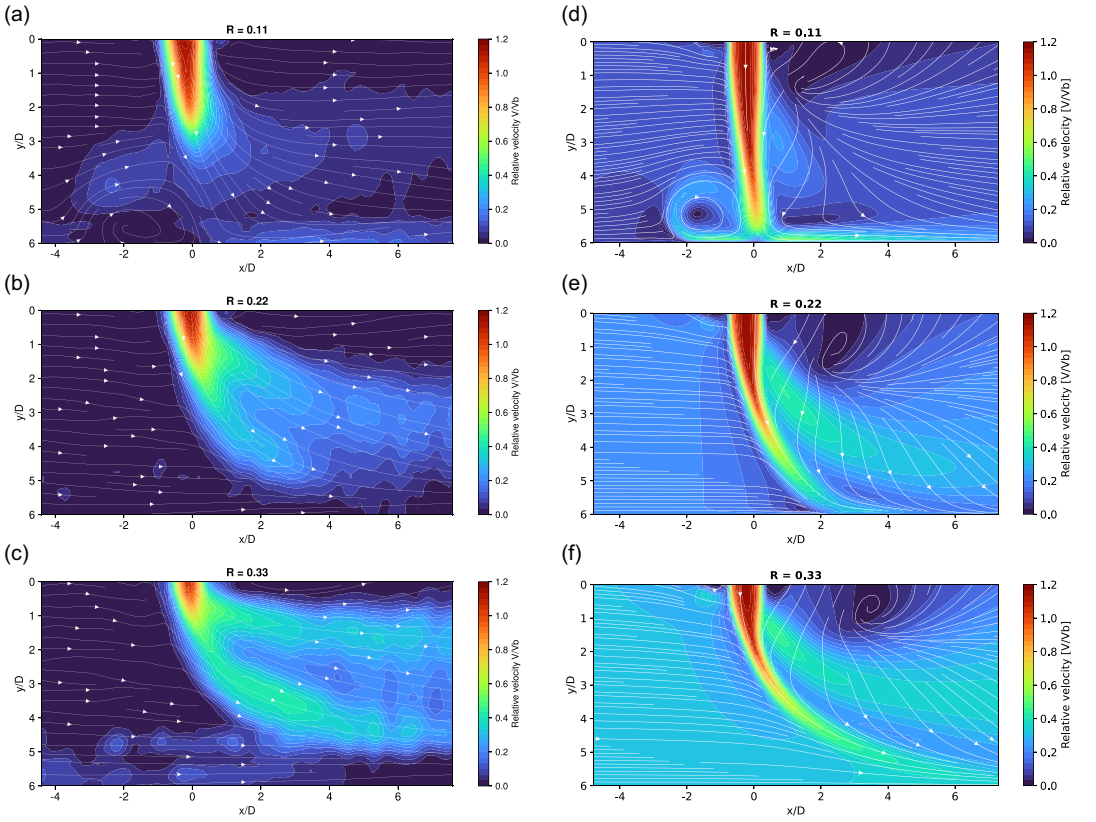

Figure 6. *Mean velocities and streamlines for multiple values of ratio R (test conditions 1, 2 and 5), both from PIV results (a–c) and numerical modelling simulations (d–f). Relative velocities are shown, thus the local velocity divided by the jet exit bulk velocity. The bed surface is located at* $y/D = 6$.

5. Results

5.1. Flow velocities and structures

Figure 6 shows the velocity fields for multiple values of the ratio R (U_t/V_b), both from PIV and the numerical model. The general topologies of the jets are similar. For the lower values of R, the circulation in front of the jet is shown by both the experimental and CFD results. The jet exit velocity profile is similar for all values of R. The split from the jet core that extends in the wake of the jet is present in both results for $R = 0.22$ and $R = 0.33$, where the split occurs closer to the jet exit for $R = 0.33$. The streamlines in the modelling results are directed downward instead of to the leeward side, as is the case for the experimental results, as the plane in the jet centreline is taken, which is where the vortices interact and the velocities are directed downward. Especially for the velocity fields close to the bed and for lower values of R, we observe larger differences between the PIV measurements and the numerical model. This is a result of a low signal-to-noise ratio most probably due to laser reflection from the table surface in the impingement region. Whereas the uncertainties are around 10% for the jet core, they are significantly larger close to the surface. In addition, the incoming velocity in the experimental results is close to zero, as the towing tank fluid did not contain enough seeding material to capture the translating velocity. The potential core is consistently shorter for the experimental results compared with the CFD results, which is especially pronounced for $R = 0.11$. For the experimental results, the jet core appears to be less than half the length of the core in the CFD simulations. The wall-jet velocities, if present, are close to zero for the experimental results, whereas we observe a significant wall jet for the model. In addition,

https://doi.org/10.1017/flo.2025.10029 Published online by Cambridge University Press

the deflection of the jet core appears to be more pronounced for the experimental results. Besides the influence of reflection, the velocities could also have been influenced by the number of particles in the interrogation window. In the jet core, the concentration of particles is high and fairly constant, whereas this quickly decreases close to the surface. This might introduce a bias in the velocities, where smaller velocities have a relative high contribution.

For all cases, the stand-off distance is $6D$. As the length of the potential is typically (4-6)D, the jets are assumed to be fully developed. For $R = 0.11$, the jet strongly impinges on the bed at $x/D \approx 0$, with a potential core that is slightly affected by the longitudinal movement and extends to $y/D = 3$. On the leeward side of the point of impingement, a wall jet develops. For a stationary jet, the flow development is axisymmetric, with undisturbed wall jets in every direction. However, the cross-flow from the translational motion forces a circulation in front of the jet. The circulation bends to both sides in a symmetrical pattern and extends in the wake of the jet (figure 7a). Close to the jet exit in the downstream region, a vortex is observed in the numerical modelling results around $y/D = 1.5$ and $x/D = 1.5$ for $R = 0.11$. This indicates the interaction between the jet shear and the downwash effect (Huang and Hsieh, 2003). There is no indication that for this ratio between the translation and jet velocities a CVP develops.

The dominance of impingement of the jet decreases when the ratio R is increased to 0.22. The jet centre streamline fully deflects to the leeward side. Even though jet impingement is still present at around $x/D = 2$, the wall jet is primarily directed to the leeward side. The jet potential core extends less into the column, to $y/D \approx 1.75$ compared with $y/D = 3$ for $R = 0.11$, and an upper plume that seems to separate from the main jet plume. The presence of an upper plume in the longitudinal plane indicates the formation of CVPs, which have the highest velocities at the jet centre streamline and at the jet centreline where the vortex pairs interact. The vortices can be observed in the coherent structures and streamlines (figure 7b) that extend far into the wake of the jet. As for $R = 0.11$, a vortex downwind of the jet exit is observed, but for $R = 0.22$ it moves slightly downstream to around $y/D = 1.5$ and $x/D = 2.5$. This movement is increased for $R = 0.33$, where it shifts to around $x/D = 3.5$. For this translation-to-jet velocity ratio, the deflection of the jet centre streamline is more pronounced, with the CVP reaching higher up in the column due to a less strong transverse motion pushing down the jet. Bed impingement is minimal, thus the jet behaves predominantly as a jet in cross-flow. Thus, the ratio R is crucial in determining the flow behaviour of the translating impinging jet.

In figures 7 and 8, the mean velocity profiles and the coherent structures for both a backward and forward directed nozzles are shown, respectively. For a backward directed jet with a jet angle of 60°, the modelling results show that the potential core reaches far into the water column with a strong wall jet to the leeward side and smooth flow structures. The potential core does not appear to be significantly affected by the translation. The flow toward the windward side is minimal, but the flow circulates in front of the main jet plume before it is deflected to the side. The wall-jet distribution on the leeward and windward sides and the bed impact depend on the jet angle (Mishra *et al.*, 2020), with more circulation in front of the jet for larger jet angles up to 90°. The flow structures for a forward pointing jet appear to be more chaotic in nature. The main wall jet is directed towards the windward side, where it interacts with the main opposing flow and is forced into a large circulation pattern. The spreading of the flow in cross-sectional direction appears to be larger and the potential core is shorter than for the vertical jet, but the deflection of the core is minimal. The flow on the leeward side is shielded by the jet plume and forward directed wall jet, thus the mean velocities are relatively small. A small circulation pattern behind the jet forms as well.

5.2. Bed pressure distribution

The pressure coefficient is significantly influenced by the following dimensionless parameters: the translation-to-jet velocity ratio (R), the stand-off distance relative to the jet diameter (H/D) and the jet angle (θ). The pressure coefficient is defined as follows:

$$C_p = \frac{P_{d,max}}{\frac{1}{2}\rho V_b^2}, \tag{7}$$

https://doi.org/10.1017/flo.2025.10029 Published online by Cambridge University Press

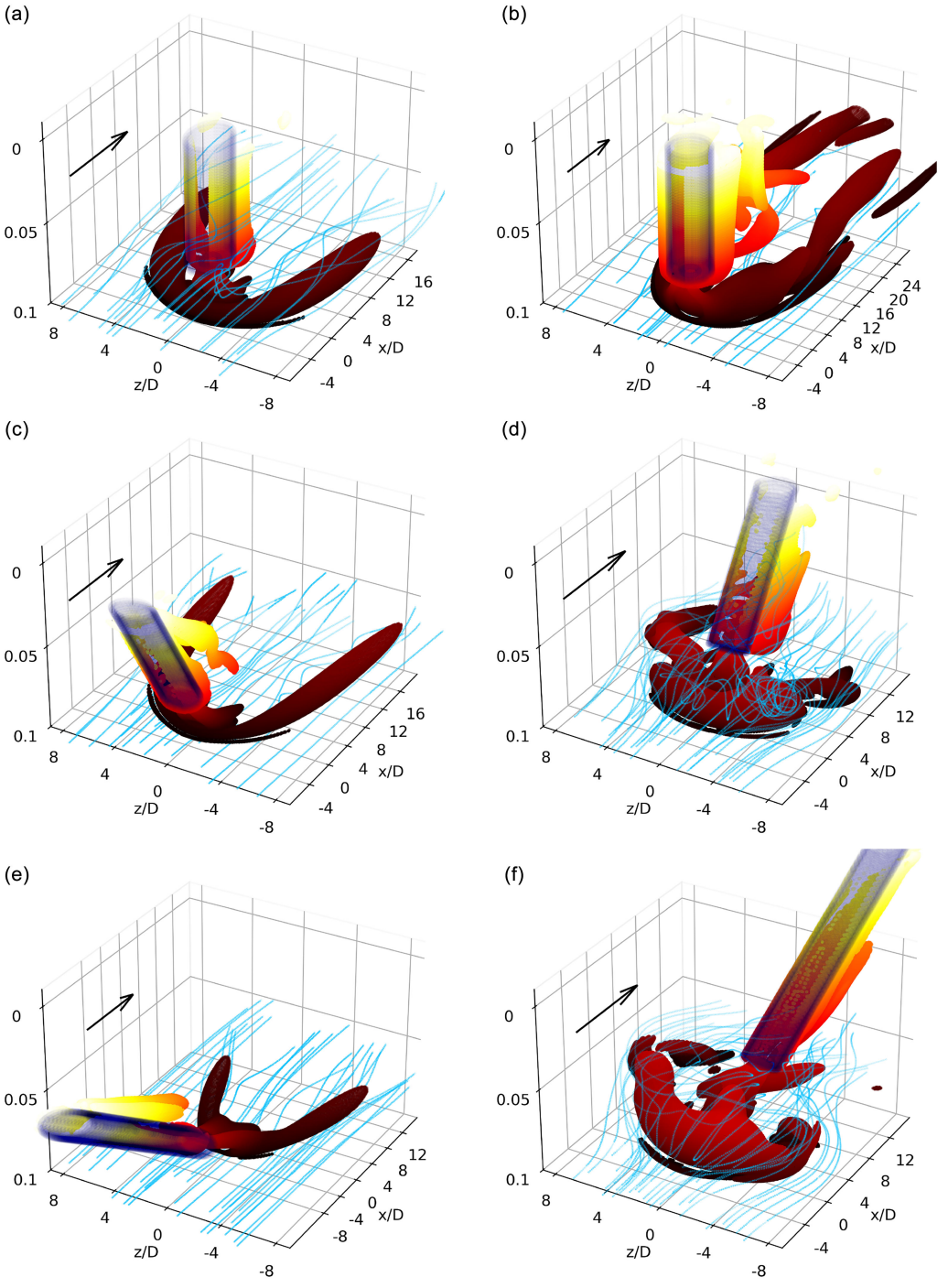

Figure 7. *Coherent structures and streamlines from CFD results for (a) ratio* $R = 0.11$ *and* $\theta = 90°$ *(test condition no. 1), (b)* $R = 0.22$ *and* $\theta = 90°$ *(no. 2), and (c)* $R = 0.11$ *and* $\theta = 60°$ *(no. 6), (d)* $\theta = 120°$ *(no. 8), (e)* $\theta = 30°$ *(no. 7), and (f)* $\theta = 150°$ *(no. 9). The structures are visualised based on* $Q = 5000$ s^{-2}*. For all y-axes,* $y = 0.07$ *is the jet exit and* $y = 0.10$ *the location of the bed. The dark blue cylinders show the nozzle. The streamlines are visualised in light blue and the structures are shown in a yellow to red scale, where the darker reds indicate structures close to the bed. The arrows show the direction of the relative cross-flow.*

https://doi.org/10.1017/flo.2025.10029 Published online by Cambridge University Press

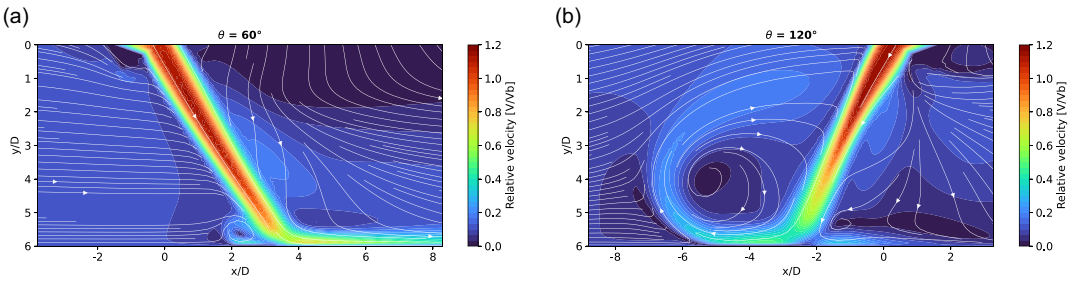

Figure 8. *Mean velocities and streamlines from CFD results for constant* $R = 0.11$ *and jet angles (a)* $\theta = 60°$ *and (b)* $\theta = 120°$*, corresponding to test conditions 6 and 8.*

where $P_{d,max}$ is the peak dynamic pressure, defined as the peak total measured pressure minus the static pressure. The relation between the pressure coefficient and ratio R is shown in figure 9a. The experimental results were extended by numerical modelling to cover the full range from $R = 0.0$ to 0.33, with the experimental results being quite close to the polynomial fit of the modelling results. The peak pressure decreases logarithmically with increasing ratio R, with approximately half of the peak pressure remaining at $R = 0.10$ compared with a stationary jet. The interaction between the moving jet and the stationary fluid will deflect the jet plume, thus affecting the potential core and length of the centre streamline (see also figure 6). The same trend is visible in the relation between the pressure coefficient and ratio H/D values over 4 (figure 9b). Up to $H/D = 4$, the peak pressure is relatively unaffected by the stand-off distance, as the potential core extends to the bed, even for $R = 0.11$. For $H/D > 4$, entrainment increases, with an logarithmically decreasing peak pressure at the bed as a result. The effect is enhanced by the presence of the relative cross-flow. The maximum pressure is registered for the vertical jet, which is equal to 90° relative to the bed (figure 9c). Notable is that, for most data points, the model slightly underestimates the bed pressure. For the jet angle of 60° the model value is approximately equal to the mean measured value. Both for increasing and decreasing angles, the pressure coefficient decreases, which can be partly explained by the additional distance to the bed. However, the decrease rates are not equal. For the two supplementary jet angles, 120° versus 60° and 150° versus 30°, the recorded pressures are higher for the backward directed jet (i.e. <90°). While the horizontal velocity component of the backward directed jet is in the same direction as the cross-flow, the forward directed jet has to counteract it. As a consequence, the velocities of the jet reaching the bed are lower. Thus, the momentum reaching the bed and applied pressure are lower.

The abovementioned pressure measurements have all been conducted in the hydraulically smooth part of the table or the CFD model without imposed roughness. Yet, three larger pressure transmitters were flush mounted in the rough section of the table to compare the pressure between the two sections. The comparison for the range of jet angles is shown in figure 9d. For the lower values of C_p, the difference is negligible. However, for jet angles of $\theta = 60°$ and 90°, the pressure measurements for the rough section are significantly higher. As the flow resistance over a hydraulically rough surface is higher and the wall-jet velocity is lower as a result, the pressure on the bed in the stagnation point might be higher compared with the situation for a smooth surface. In the absence of a clear stagnation point, as is especially the case for $\theta = 30°$ and 120°, the difference might be minimal.

In addition to the maximum bed pressure, the model can also provide the pressure distribution at the bed boundary. For a jet with $R = 0.11$ (figure 10a), the higher pressures are concentrated, with the pressure area having a kidney shape and a slight area of negative pressure in front of the jet. For increasing values of R, the pressure area becomes more widespread, especially on the leeward side (figure 10b). However, the pressure coefficients are significantly lower. The kidney-shaped area deflects towards the leeward side for the backward directed jet with the pressure profile being more compact overall, in figure 10c the bed pressure for a jet angle of 60° is shown. The spreading is limited when the angle is further reduced to 30° (figure 10e). The pressure distribution shows a less coherent pattern for the forward directed jet (figure 10d). The distribution appears asymmetric, as the steady-state model does not

https://doi.org/10.1017/flo.2025.10029 Published online by Cambridge University Press

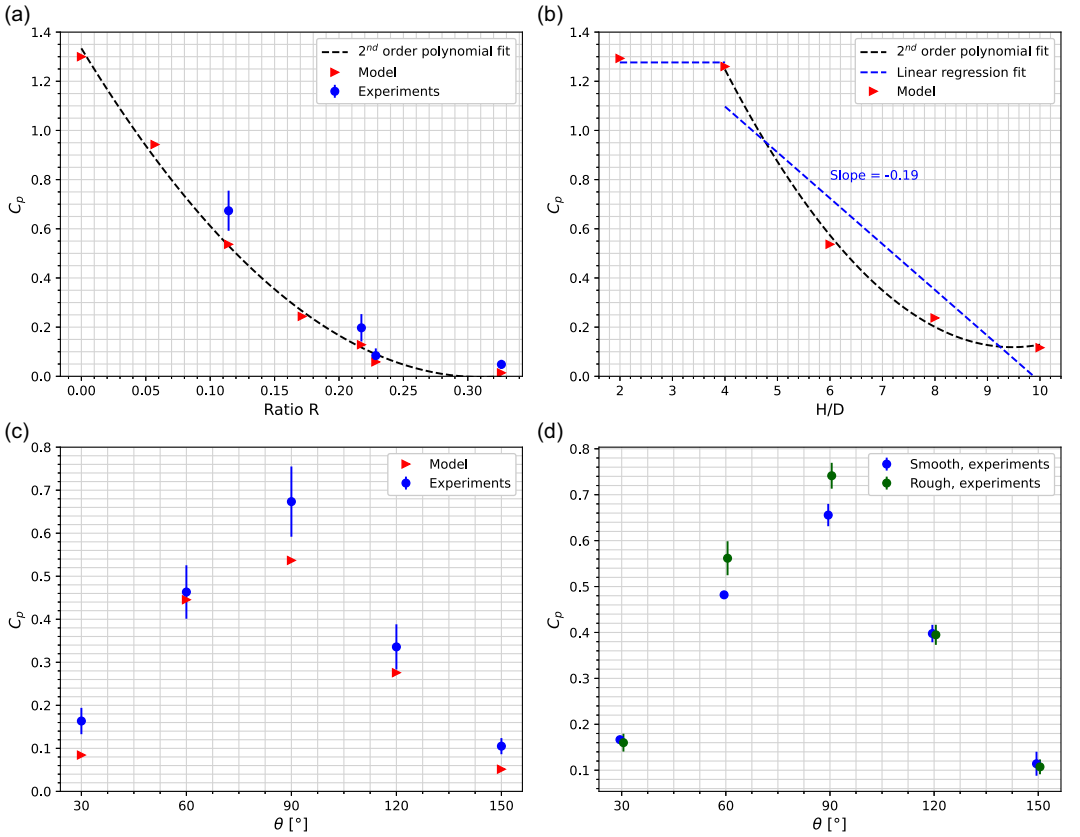

Figure 9. *Relation between the pressure coefficient C_p and the translation-to-jet velocity ratio R for constant $\theta = 90°$ (a), stand-off distance to jet diameter ratio H/D for constant $R = 0.11$ (b) and the jet angle θ for constant $R = 0.11$ and $H/D = 6$ (c). In addition, for the relation between C_p and θ, the pressure measurements for the hydraulically smooth and rough parts of the table are shown (d).*

converge due to the highly turbulent nature of the circulation in front of the jet. The pressure coefficient is significantly higher for its supplementary jet angle (60°, figure 10c). The same trend is observed when the jet angle is further increased (figure 10f), with a minimal pressure coefficient. Except for the pressure distribution for $R = 0.22$, for which the spreading is slightly different, overall, the pressure area is limited to $0 \leq x/D \leq 2$ and $-2 \leq z/D \leq 2$.

6. Discussion

Our research focused on the effect of three dimensionless parameters on the velocity field and bed pressure distribution of submerged translating inclined impinging water jets, namely the translation-to-jet velocity ratio R, the stand-off distance to jet diameter ratio H/D and the jet angle θ. For stationary impinging jets, numerous studies have investigated the influence of ratio H/D (Hammad and Milanovic, 2011; Liu *et al.*, 2023; Wang *et al.*, 2015) and jet angle θ (Mishra *et al.*, 2020; Wang *et al.*, 2017; Zhang *et al.*, 2022). The research on the flow field of translating jets is limited, but erosion studies have already documented the importance of the translation-to-jet velocity ratio R, with a nonlinear relation between the erosion depth and the ratio (Wang *et al.*, 2021; Yeh *et al.*, 2009; Zhang *et al.*, 2016). While the pressure and erosion depth cannot be compared directly and erosion is additionally affected by the contact time, our results clearly show that the bed pressure is inversely related to ratio R due to the increased deflection of the jet centre. For ratio H/D, we have observed two regimes. For $H/D < 4$, the flow is

https://doi.org/10.1017/flo.2025.10029 Published online by Cambridge University Press

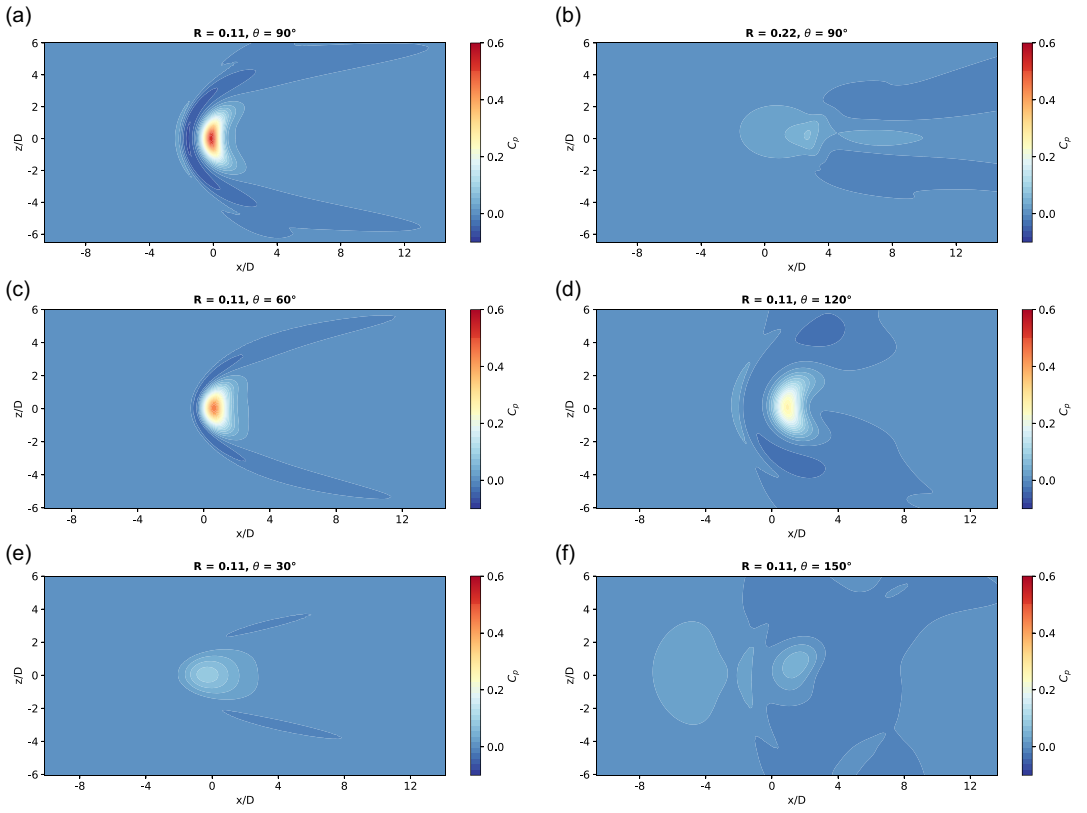

Figure 10. *Pressure distribution for vertical jets with $R = 0.11$, test condition 1 (a) and $R = 0.22$, condition 2 (b) and inclined jets with $\theta = 60°$, condition 6 (c) $\theta = 120°$, condition 8 (d), $\theta = 30°$, condition 7 (e) and $\theta = 150°$, condition 9 (f), all with $R = 0.11$. Here, $x/D = 0$ indicates the position of the geometric centre. For all simulations, the ratio H/D was equal to 6.*

dominated by the jet, with a minimal decrease in bed pressure. When $H/D > 4$, the potential core has diminished and the influence of the relative cross-flow increases. Therefore, the slope of the linear regression is steeper compared with the one found by Wang *et al.* (2015), who studied a stationary vertical impinging jet. The velocity fields for an inclined jet can be compared with the stationary jet studies of Mishra *et al.* (2020) and Wang *et al.* (2017) to a certain extent, as our study also shows that the jet angle θ affects the dominant wall-jet direction. However, the relative cross-flow introduces a circulation in front of the jet that is naturally not observed for stationary jets. The pressure coefficient of Wang *et al.* (2017) shows a similar trend to our experimental findings for $30° \leq \theta \leq 90°$. However, our pressure values are relatively smaller. As for the ratio H/D, the relative cross-flow might further enhance the velocity reduction close to the bed.

The results from the numerical model were compared with the experimental results to assess its overall performance. Our hypothesis is that translation of the jet through a stagnant medium, as is used for the experimental set-up, and a stationary jet in a cross-flow, as is the case in the numerical model, are interchangeable. The approach of a stationary jet in cross-flow significantly reduces the complexity of the model compared with one with a dynamic mesh. The minimal differences in maximum bed pressures and jet core velocities show that this assumption holds, at least for the general flow characteristics. We were aiming to also visualise the flow structures close to the surface, but it was difficult to obtain reliable PIV measurements close to the surface due to the unwanted reflections of light from the table. This especially affected the relatively small out-of-plane velocities, which are of great interest in this region as the impingement region of the jet is highly three-dimensional. For future research, a fixed PIV

https://doi.org/10.1017/flo.2025.10029 Published online by Cambridge University Press

system might be preferable over the moving set-up we used for this study, with the downside of needing many repetitions for statistical averaging. However, based on the results we are confident that the model manages to capture the dominant flow characteristics.

7. Conclusions

In this study, we combined experimental and numerical results to investigate the flow field of submerged translating inclined impinging water jets using underwater stereoscopic PIV and pressure measurements, as well as a validated OpenFOAM model. We studied the effect of multiple dimensionless jet parameters, including the jet angle θ, the stand-off distance to jet diameter ratio H/D and the translation-to-jet velocity ratio R, on the flow characteristics and maximum bed pressure. In addition, we found that the computationally efficient steady-state RANS model manages to capture the dominant flow characteristics of a translating impinging jet.

The jet angle affects the distribution of the flow. The wall-jet distribution and strength of the circulation pattern in front of the translating jet depend on the jet being backward, $\theta < 90°$, or forward, $\theta > 90°$, directed. The flow structures of a backward directed jet resemble those of a vertical jet, albeit slightly smoother. The circulation in front of the translating jet increases significantly when considering a forward directed jet, with a wider spreading of the flow. Bed pressures are unequal for supplementary jet angles (e.g. 60° and 120°), with higher pressures recorded for a backward directed jet.

The stand-off distance to nozzle diameter ratio *H/D* determines the governing flow mechanism. For $R = 0.11$, the jet flow is relatively unaffected by the presence of the cross-flow up to $H/D = 4$. When the ratio H/D is larger than 4, the potential core no longer extends to the bed and entrainment increases, thus the peak pressure will decrease exponentially. This effect is enhanced by the relative cross-flow.

Lastly, the translation-to-jet velocity ratio R is an important dimensionless parameter in determining the flow characteristics. Jet impingement is dominant for relatively small values of R, with a strong wall-jet flow along the bed, where the upstream flow is forced into circulation by the relative cross-flow. Approximately half of the peak stagnation pressure remains for $R = 0.10$ for the considered test conditions. We found that for $R > 0.22$, jet impingement is minimal and the jet flow behaves predominantly as a jet in cross-flow with its characteristic CVP. For applications requiring strong jet impingement, a sufficiently small value of velocity ratio R is crucial.

Acknowledgments. The authors are grateful to S. Schreier and G. Jacobi for their help on the conceptualisation of the experimental set-up. In addition, the authors would like to thank the technical staff of the Ship Hydrodynamics Lab at Delft University of Technology for their assistance with the set-up.

Funding statement. The authors gratefully acknowledge funding by NWO. This publication was conducted as part of the StimTech project (TTW-19231), which falls under the programme Research towards Sustainable Fisheries (RSF). Open access funding provided by Delft University of Technology.

Declaration of interests. The authors declare no conflict of interest.

Author contributions. S.V. Bult: Conceptualisation, Methodology, Investigation, Writing – Original Draft, Visualisation, Software, Formal analysis. S. Tokgoz: Methodology, Investigation, Writing – Review & Editing. S. Alhaddad: Conceptualisation, Methodology, Supervision. R. Helmons: Writing – Review & Editing, Supervision. G.H. Keetels: Conceptualisation, Methodology, Writing – Review & Editing, Supervision, Project Administration, Funding acquisition.

Data availability statement. Data and code can be requested from the corresponding author (S.V.B.).

References

Adrian, R. J., & Westerweel, J. (2011). *Particle image velocimetry*. Cambridge University Press.

Alhaddad, S., Snyder, A., Bult, S. V., & Keetels, G. H. (2025). Experimental investigation of cohesive soil erosion caused by translating submerged inclined water jets. *Applied Ocean Research*, *157*, 104486. 10.1016/j.apor.2025.104486.

https://doi.org/10.1017/flo.2025.10029 Published online by Cambridge University Press

Beltaos, S. (1976). Oblique impingement of circular turbulent jets. 10.1080/00221687609499685.
Coletti, F., Benson, M. J., Ling, J., Elkins, C. J., & Eaton, J. K. (2013). Turbulent transport in an inclined jet in crossflow. *International Journal of Heat and Fluid Flow*, *43*, 149–160. 10.1016/j.ijheatfluidflow.2013.06.001.
de Wit, L., Talmon, A. M., & van Rhee, C. (2014). 3d cfd simulations of trailing suction hopper dredger plume mixing: Comparison with field measurements. *Marine Pollution Bulletin*, *88*, 34–46. 10.1016/j.marpolbul.2014.08.042.
de Wit, L., van Rhee, C., & Talmon, A. (2015). Influence of important near field processes on the source term of suspended sediments from a dredging plume caused by a trailing suction hopper dredger: The effect of dredging speed, propeller, overflow location and pulsing. *Environmental Fluid Mechanics*, *15*, 41–66. 10.1007/s10652-014-9357-0.
Deo, R. C., Mi, J., & Nathan, G. J. (2008). The influence of Reynolds number on a plane jet. *Physics of Fluids*, *20*, 075108. 10.1063/1.2959171.
Dong, C., Yu, G., Zhang, H., & Zhang, M. (2020). Scouring by submerged water jet vertically impinging on a cohesive bed. *Ocean Engineering*, *196*, 106781. 10.1016/j.oceaneng.2019.106781.
Fairweather, M., & Hargrave, G. K. (2002). Experimental investigation of an axisymmetric, impinging turbulent jet. 1. velocity field. *Experiments in Fluids*, *33*, 464–471. 10.1007/s00348-002-0479-7.
Fitzgerald, J. A., & Garimella, S. V. (1998). A study of the flow field of a confined and submerged impinging jet. *International Journal of Heat Mass Transfer*, *41*, 1025–1034.
Fric, T. F., & Roshko, A. (1994). Vortical structure in the wake of a transverse jet. *Journal of Fluid Mechanics*, *279*, 1–47. 10.1017/S0022112094003800.
Gevorkyan, L., Shoji, T., Gestinger, D. R., Smith, O. I., & Karagozian, A. R. (2016). Transverse jet mixing characteristics. *Journal of Fluid Mechanics*, *790*, 237–274. 10.1017/jfm.2016.5.
Hammad, K. J., & Milanovic, I. (2011). Flow structure in the near-wall region of a submerged impinging jet. *Journal of Fluids Engineering*, *133*, 091205. 10.1115/1.4004907.
Hassan, M. E., Assoum, H. H., Martinuzzi, R., Sobolik, V., Abed-Meraim, K., & Sakout, A. (2013). Experimental investigation of the wall shear stress in a circular impinging jet. *Physics of Fluids*, *25*. 10.1063/1.4811172.
He, G., Guo, Y., & Hsu, A. T. (1999). The effect of schmidt number on turbulent scalar mixing in a jet-in-crossflow. *International Journal of Heat and Mass Transfer*, *42*, 3727–3738. 10.1016/S0017-9310(99)00050-2.
Huang, R. F., & Hsieh, R. H. (2003). Sectional flow structures in near wake of elevated jets in crossflow. *AIAA Journal*, *41*, 1490–1499. 10.2514/2.2099.
Jacobi, G., Thill, C. H., & Huijsmans, R. H. (2022). Pressure reconstruction from piv measurements in the bow region of a fast ship. *Ocean Engineering*, *252*, 110318. 10.1016/j.oceaneng.2021.110318.
Jacobi, G., Thill, C. H., van't Veer, R., & Huijsmans, R. H. (2019). Analysis of the influence of an interceptor on the transom flow of a fast ship by pressure reconstruction from stereoscopic scanning piv. *Ocean Engineering*, *181*, 281–292. 10.1016/j.oceaneng.2019.02.062.
Jalil, A., & Rajaratnam, N. (2006). Oblique impingement of circular water jets on a plane boundary. *Journal of Hydraulic Research*, *44*(6), 807–814. 10.1080/00221686.2006.9521731.
Jiang, T., Huang, Z., Li, J., Zhou, Y., & Xiong, C. (2022). Effect of nozzle geometry on the flow dynamics and resistance inside and outside the cone-straight nozzle. *ACS Omega*, *7*, 9652–9665.
Liu, X., Chen, X., Wei, J., Jin, S., Gao, X., Sun, G., Yan, J., & Lu, Q. (2023). Study on sediment erosion generated by a deep-sea polymetallic-nodule collector based on double-row jet. *Ocean Engineering*, *285*, 115220. 10.1016/j.oceaneng.2023.115220.
Lu, Y., Tang, J., Ge, Z., Xia, B., & Liu, Y. (2013). Hard rock drilling technique with abrasive water jet assistance. *International Journal of Rock Mechanics and Mining Sciences*, *60*, 47–56. 10.1016/j.ijrmms.2012.12.021.
Mahesh, K. (2013). The interaction of jets with crossflow. *Annual Review of Fluid Mechanics*, *45*, 379–407. 10.1146/annurev-fluid-120710-101115.
Menter, F. R. (1994). Two-equation eddy-viscosity turbulence models for engineering applications. *AIAA Journal*, *32*, 1598–1605. 10.2514/3.12149.
Mishra, A., Yadav, H., Djenidi, L., & Agrawal, A. (2020). Experimental study of flow characteristics of an oblique impinging jet. *Experiments in Fluids*, *61*, 90. 10.1007/s00348-020-2923-y.
Nobel, A. J. (2013). *On the excavation process of a moving vertical jet in cohesive soil* (Doctoral dissertation). Delft University of Technology.
Oranli, E., Gungoren, N., Astaraee, A. H., Maleki, E., Bagherifard, S., & Guagliano, M. (2023). Numerical and experimental analysis of sand blasting on polymeric substrates. *Forces in Mechanics*, *12*, 100208. 10.1016/j.finmec.2023.100208.
Paterna, E., Moonen, P., Dorer, V., & Carmeliet, J. (2013). Mitigation of surface reflection in piv measurements. *Measurement Science and Technology*, *24*, 057003. 10.1088/0957-0233/24/5/057003.
Schlichting, H. (1979). *Boundary-layer theory*. McGraw-Hill.
Smith, S. H., & Mungal, M. G. (1998). Mixing, structure and scaling of the jet in crossflow. *Journal of Fluid Mechanics*, *357*, 83–122. 10.1017/S0022112097007891.
Van Raalte, G. H., & Bray, R. (1999). Hydrodynamic dredging: Principles, effects and methods. In *Dredging challenged. Proceedings of the CEDA Dredging Days*.
Wang, B., van Rhee, C., Nobel, A., & Keetels, G. (2021). Modeling the hydraulic excavation of cohesive soil by a moving vertical jet. *Ocean Engineering*, *227*, 108796.

Wang, C., Wang, X., Shi, W., Lu, W., Tan, S. K., & Zhou, L. (2017). Experimental investigation on impingement of a submerged circular water jet at varying impinging angles and reynolds numbers. *Experimental Thermal and Fluid Science*, *89*, 189–198. 10.1016/j.expthermflusci.2017.08.005.

Wang, X. K., Niu, G.-P., Y., S.-Q., Zheng, J. X., & Tan, S. K. (2015). Experimental investigation on the mean flow field and impact force of a semi-confined round impinging jet. *Fluid Dynamics Research*, *47*, 025501. 10.1088/0169-5983/47/2/025501.

Westerweel, J., & Scarano, F. (2005). Universal outlier detection for piv data. *Experiments in Fluids*, *39*, 1096–1100. 10.1007/s00348-005-0016-6.

Yeh, P. H., Chang, K. A., Henriksen, J., Edge, B., Chang, P., Silver, A., & Vargas, A. (2009). Large-scale laboratory experiment on erosion of sand beds by moving circular vertical jets. *Ocean Engineering*, *36*, 248–255. 10.1016/j.oceaneng.2008.11.006.

Zhang, D., Wang, H., Liu, J., Wang, C., Ge, J., Zhu, Y., Chen, X., & Hu, B. (2022). Flow characteristics of oblique submerged impinging jet at various impinging heights. *Journal of Marine Science and Engineering*, *10*, 399. 10.3390/jmse10030399.

Zhang, S., Zhao, M., Ge, T., & Wang, C. (2016). Experimental research on trenching in stiff clay by submerged vertical traveling jets. *Journal of Coastal Research*, *32*, 365–373. 10.2112/JCOASTRES-D-14-00038.1.

Zhang, Z., Kuang, J., Chen, G., Zeng, H., Huang, B., & Liu, Z. (2024). Numerical study on trenching performances of the underwater jet flow for submarine cable laying. *Applied Ocean Research*, *150*, 104140. 10.1016/j.apor.2024.104140.

Cite this article: Bult S. V., Tokgoz S., Alhaddad S., Helmons R. and Keetels G. H. (2025). Experimental and numerical flow field study of submerged translating impinging inclined water jets. *Flow*, *5*, E36. https://doi.org/10.1017/flo.2025.10029